nature communications

Article

https://doi.org/10.1038/s41467-025-61320-0

Enhanced catalytic activity on atomically dispersed $PtSe_2$ two-dimensional layers

Received: 4 September 2024

Accepted: 16 June 2025

Published online: 03 July 2025

Check for updates

Gyuho Han[1,10], Hyuk Choi[2,10], Jong Hun Kim[3,4,10], Daeho Kim[1], Sang Sub Han[5], Hyewon Park[1], Si Woo Lee[6], Ki-jeong Kim[7], Jeongjin Kim[7], Min Gyu Kim[7], Yeonwoong Jung[5,8,9] ✉, Hyun You Kim[2] ✉ & Jeong Young Park[1] ✉

A key challenge in heterogeneous catalysis is to design atomically dispersed catalysts with high surface density, while simultaneously preventing agglomeration and promoting electronic metal-support interaction. Transition metal dichalcogenides (TMDs), such as platinum diselenide ($PtSe_2$), offer a promising solution due to their unique structural and electronic properties. This study proposes a catalyst design that utilizes atomically dispersed transition metal species within the topmost layer of TMD as catalytic reaction sites. The substantial presence of surface-exposed Pt species on $PtSe_2$ and their role as catalytic reaction sites are elucidated using *operando* ambient-pressure X-ray photoelectron spectroscopy. Moreover, significantly high O_2 coverage on $PtSe_2$, achieved by mitigating the exclusive adsorption of carbon monoxide (CO), leads to enhanced CO oxidation performance. The characteristic *d*-band structure and resulting high O_2 coverage of $PtSe_2$ are further confirmed with density functional theory calculations. Overall, this study highlights the potential of densely distributed atomic transition metal on TMDs, which allows electronic metal-chalcogen interactions and diverse reaction mechanisms.

Designing a catalyst to intensify performance at each reaction site is a fundamental challenge in heterogeneous catalysis. This efforts has led to a reduction in the size of metal catalysts to increase surface free energy and expose a greater number of reaction sites on the surface, eventually resulting in the development of atomic catalysts[1,2]. Moreover, reducing the size to the atomic level enables metal catalysts to facilitate charge transfer through interaction with supporting materials[3,4]. This electronic metal-support interaction (EMSI) significantly alters the charge distribution of atomic catalysts and manipulates catalytic properties, such as binding energies of distinct adsorbates and activation energies, thereby enhancing catalytic performances[5–8]. However, designing atomically dispersed catalysts with high-density remains challenging, as metal atoms are prone to agglomeration and restructuring into nanoclusters during synthesis and reaction due to their high surface free energy[9–11]. As a result, excessive distance between metal atoms limits the ability to follow diverse reaction mechanisms and reduces overall catalytic activity[12–14].

In this study, we propose a unique approach to address the issue of dense distribution by utilizing the metal element composing the transition metal dichalcogenide (TMD) as reaction sites in a solid-gas system. In heterogeneous catalysis, research on TMDs has been mainly focused on their capability as catalyst support, which effectively stabilizes atomic catalysts[15–18]. However, employing TMDs themselves as a catalyst allows us to utilize the densely distributed metal atoms. In the

[1]Department of Chemistry, Korea Advanced Institute of Science and Technology (KAIST), Daejeon, Republic of Korea. [2]Department of Materials Science and Engineering, Chungnam National University, Daejeon, Republic of Korea. [3]Department of Materials Science and Engineering, Seoul National University, Seoul, Republic of Korea. [4]Department of Physics, Inha University, Incheon, Republic of Korea. [5]NanoScience Technology Center, University of Central Florida, Orlando, FL, USA. [6]Department of Chemical Engineering, Inha University, Incheon, Republic of Korea. [7]Pohang Accelerator Laboratory, Pohang University of Science and Technology (POSTECH), Pohang, Gyeongbuk, Republic of Korea. [8]Department of Electrical and Computer Engineering, University of Central Florida, Orlando, FL, USA. [9]Department of Materials Science and Engineering, University of Central Florida, Orlando, FL, USA. [10]These authors contributed equally: Gyuho Han, Hyuk Choi, Jong Hun Kim. ✉e-mail: yeonwoong.jung@ucf.edu; kimhy@cnu.ac.kr; jeongypark@kaist.ac.kr

case of $PtSe_2$, surface-exposed Pt atoms, formed due to Se vacancies, can interact with reactants and act as catalytic reaction sites[19]. Mono- or few-layer $PtSe_2$ with Se-vacancy can be synthesized by selenizing Pt under a high vacuum or H_2/Ar gas flow[20,21]. Since Se-vacancy has a low formation energy over a wide range of Se chemical potential, the formation of $PtSe_2$ with substantial exposure of Pt atoms on the surface is likely[22]. In this configuration, Pt atoms form somewhat looser arrangements than those in Pt(111). Nevertheless, since Pt atoms are not too far apart, adsorbates can adsorb on various exposed Pt sites, such as atop, bridge, and hollow sites. Moreover, catalytic reactions can follow various catalytic mechanisms, such as the Langmuir-Hinshelwood (LH) mechanism, due to the interaction between adsorbates adsorbed on adjacent Pt sites.

The TMD catalyst also allows us to manipulate the electronic structure of the atomic catalyst through charge transfer between metal and chalcogen, thereby enhancing catalytic performance. Regarding the carbon monoxide (CO) oxidation reaction on Pt as a representative, there are difficulties due to the differences in binding energy between CO and O_2[23,24]. For optimal catalytic activity, CO and O_2 should be adsorbed on the surface of platinum in adequate proportions. However, the binding energies of CO and O_2 on the Pt(111) are −1.77 eV and −1.10 eV, respectively, making the adsorption of CO significantly stronger than O_2. Consequently, the exclusive adsorption of CO inhibits the O_2 adsorption and reduces catalytic activity while following the LH mechanism, known as the CO poisoning effect[25,26]. Nevertheless, by utilizing Pt atoms in $PtSe_2$ as a catalyst, we can modulate the *d*-band center (ε_d) through Pt-Se charge transfer. According to *d*-band theory, the binding energy of adsorbate is closely related to the extent to which electrons are filled in the antibonding state of the metal-adsorbate bond. When the ε_d is lowered, the antibonding state also decreases, allowing more electrons to be filled and weakening the binding energy[27]. Therefore, the electronic metal-chalcogen interaction enables us to weaken the binding energy of CO significantly. The manipulation of the binding energy of CO and O_2 induces resistance to the CO poisoning and highly increases the coverage of O_2, thereby promoting rapid interaction between them.

Considering these factors, we showcase the potential of $PtSe_2$ as a heterogeneous catalyst in a solid-gas system by utilizing atomically dispersed Pt as an active catalytic site under the CO oxidation reaction. Using *operando* ambient-pressure X-ray photoelectron spectroscopy (AP-XPS), we identified the sufficient exposure of Pt on the surface (i.e., Se-vacancy) and its function as catalytic reaction sites. Moreover, we elucidated the electronic metal-chalcogen interaction between Pt and Se and its role on CO oxidation through density functional theory (DFT) calculations. Subsequent experimental and theoretical comparisons with Pt(111) elucidate the superior catalytic performance of $PtSe_2$ due to its significantly high O_2 coverage and densely distributed Pt atoms on the surface.

Results

Synthesis and characterization of high-quality $PtSe_2$

To synthesize $PtSe_2$ multilayer, Pt film with a thickness of 0.75 nm was deposited on a SiO_2/Si substrate using an e-beam evaporator. Subsequently, Pt film was selenized via a chemical vapor deposition (CVD) method. The synthesized $PtSe_2$ showed a 1T-hexagonal structure, which can be differentiated into Se-Pt-Se sublayers, as shown in Fig. 1a[28]. The structure of $PtSe_2$ was characterized by cross-sectional high-angle annular dark-field scanning transmission electron microscopy (HADDF-STEM) and bright-field high-resolution transmission electron microscopy (HRTEM). The STEM image in Fig. 1b shows the atomically dispersed nature of Pt with appropriate distance for catalytic reaction requiring multiple adsorption sites while supported by Se atoms in the upper and lower sublayers. The corresponding energy-dispersive X-ray spectroscopy (EDS) was performed to show the elemental distribution of synthesized $PtSe_2$ (Supplementary Fig. 1)[29]. The HRTEM image in Fig. 1c shows that the multilayer $PtSe_2$ is well resolved to parallel the underlying SiO_2 substrate. The van der Waals (vdW) gap was observed via the corresponding fast Fourier transform (FFT) pattern with a spacing of ~0.55 nm, consistent with the previously reported interlayer spacing of $PtSe_2$ along the (001) direction[20,30].

The bonding characteristics and electronic structure of $PtSe_2$ were investigated using Pt L3 edge X-ray absorption spectroscopy (XAS), in comparison with the spectra of metallic Pt and PtO_2. The XAS data were normalized using the signal from a standard Pt foil. In the X-ray absorption near-edge structure (XANES) spectrum, the whiteline intensity of $PtSe_2$ was measured to be 1.66, which lies between that of metallic Pt (1.29) and PtO_2 (2.02) (Fig. 1d). The L3 edge peak position of $PtSe_2$ (11567.5 eV) also appeared at a slightly higher photon energy than that of metallic Pt (11567.1 eV), but lower than that of PtO_2 (11568.1 eV). The increase in whiteline intensity is known to indicate a higher number of unoccupied 5*d* states, whereas the peak shift reflects an increased energy separation between the $2p_{3/2}$ core level and the 5*d* orbitals[31,32]. Together, these observations indicate that the Pt atoms in $PtSe_2$ are moderately oxidized, which enables fine-tuning of the binding energies of gas molecules adsorbed on Pt sites[33].

To further investigate the local coordination environment of Pt in $PtSe_2$, extended X-ray absorption fine structure (EXAFS) analysis was performed (Fig. 1e). The EXAFS spectra were obtained by k^3-weighted Fourier transform (FT) over a k-range of 3.0 to 12.0 $Å^{-1}$. The $PtSe_2$ spectra exhibited a single prominent peak at 2.16 Å, corresponding to the Pt-Se bond. In addition, comparison with the spectra from metallic Pt revealed that peaks corresponding to Pt-Pt bonds (2.35 and 2.93 Å) were not observed in the $PtSe_2$ spectra. These results indicate that the catalytic performance of $PtSe_2$ does not originate from undesired bonding or phases such as Pt nanoclusters, but rather from surface-exposed Pt atoms at the Se vacancies in the topmost Se sublayer[19,34].

CO oxidation properties and structural stability

The catalytic performance of the $PtSe_2$ was evaluated in an ultrahigh vacuum (UHV) batch reactor under the CO oxidation reaction[35]. As a reference sample, Pt film with a thickness of 20 nm was also prepared using an e-beam evaporator. We performed the CO oxidation reaction as a model reaction in the batch reactor from 180 °C to 220 °C under 40 Torr of CO, 100 Torr of O_2, and 620 Torr of He to match the total pressure to the atmospheric pressure. Catalytic activities of $PtSe_2$ and Pt film were evaluated with turnover frequency (TOF) as a function of temperature (Fig. 2a). As a result, $PtSe_2$ showed higher catalytic activity compared to Pt over the entire temperature range, particularly 3.26 times higher from 92.4 ± 0.4 to 301.1 ± 19.3 at 220 °C. The average TOF values were replotted on the logarithmic-Arrhenius scale, as shown in Fig. 2b. The activation energies (E_a), derived from the slopes of the Arrhenius plots, were 19.3 and 17.8 kcal/mol for $PtSe_2$ and Pt, respectively. These E_a values show only marginal differences compared to the variation in TOF, suggesting that E_a value is not the primary factor influencing the differences in catalytic performance. The similar E_a values also suggest that the reaction mechanism on $PtSe_2$ might be similar to that on Pt. It is well known that CO oxidation on Pt follows the LH mechanism, indicating that CO oxidation on $PtSe_2$ likely involves two or more adjacent Pt sites[23]. To further verify the stable catalytic performance of $PtSe_2$, we conducted repeated tests that yielded consistent TOF values (51.7 ± 0.3 at 180 °C) and E_a values (19.3 ± 1.1 kcal/mol) based on Arrhenius plots (Supplementary Figs. 2a, b and 3). In the separate long-term test, the TOF remained stable over 10 hours, further confirming the durability of $PtSe_2$ (Supplementary Fig. 2c, d).

Moreover, TOF of $PtSe_2$ and Pt film were evaluated while changing the CO partial pressure, with the O_2 partial pressure fixed at 100 Torr (Fig. 2c). The TOF of $PtSe_2$ showed a slight decrease with increasing CO partial pressure, whereas the TOF of Pt decreased rapidly. This trend arises as the adsorption of O_2 becomes more difficult with the

https://doi.org/10.1038/s41467-025-61320-0

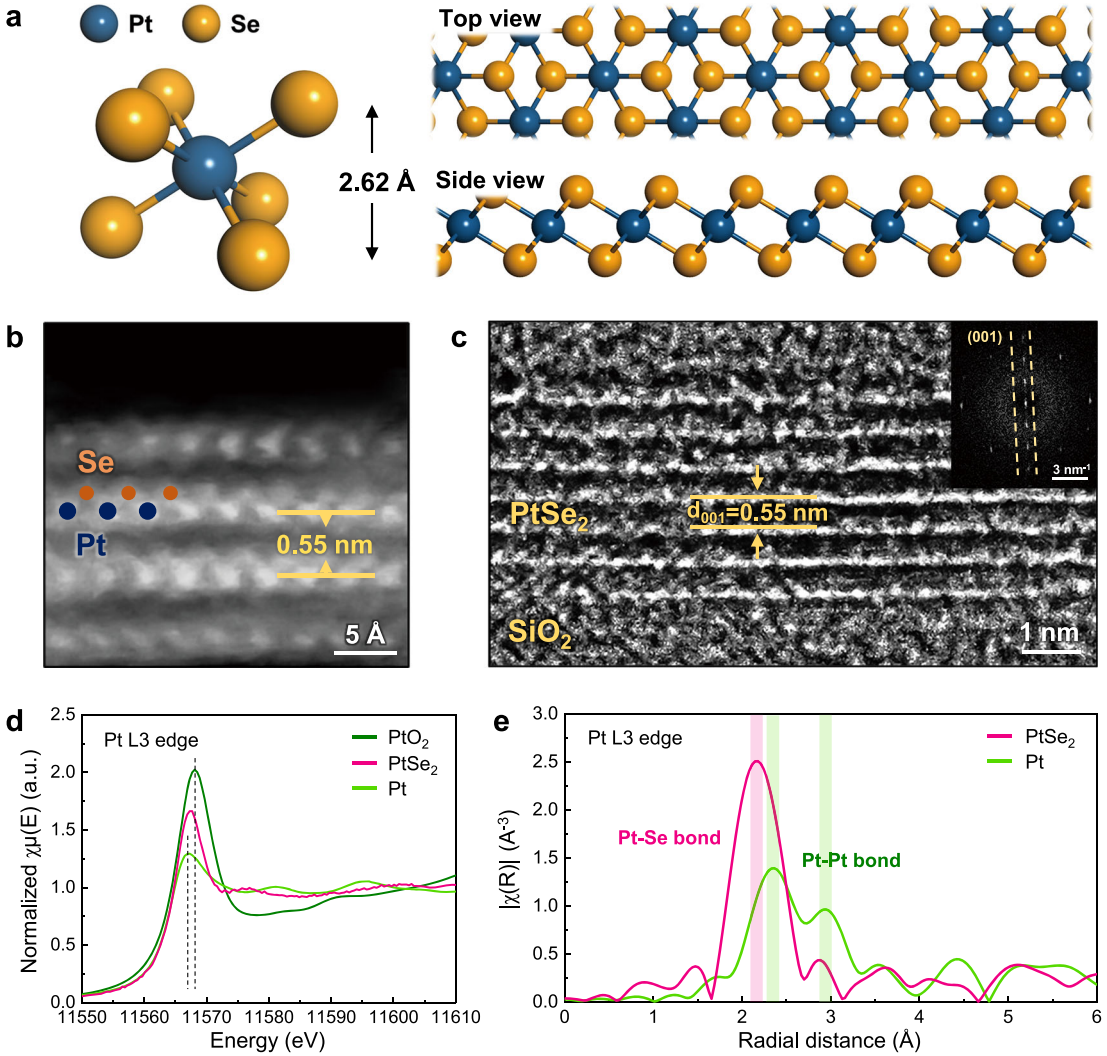

Fig. 1 | Structural characterizations of as-deposited $PtSe_2$. **a** Geometric scheme of $PtSe_2$ unit cell with top-view and side-view of $PtSe_2$ layer. **b** Cross-sectional HAADF-STEM image of $PtSe_2$ deposited on the SiO_2/Si film. **c** Cross-sectional HRTEM image and corresponding FFT pattern of $PtSe_2$. **d** Pt L3 edge XAS spectra and **e** corresponding FT-EXAFS spectra of $PtSe_2$, with Pt and PtO_2 as references.

increasing partial pressure of CO, thereby reducing the likelihood of CO reacting with the adsorbed oxygen[24]. Therefore, the gradual decrease trend of $PtSe_2$ verifies its high resistance to CO poisoning and implies that the binding energy of O_2 is similar to that of CO. Since the binding energy of adsorbate is closely related to the charge transfer through a metal-chalcogen bond, it can be inferred that the binding energies of CO and O_2 on $PtSe_2$ were affected by the charge transfer through the Pt-Se bond[5]. Investigations on the charge transfer and surface coverage of reactant molecules will be explained further with DFT calculations.

To analyze possible structural variations and their impact on catalytic activity, structural characterizations of $PtSe_2$ were conducted. The crystal structure of $PtSe_2$ was explored by X-ray diffraction (XRD) at the macroscale. As shown in Fig. 2d, a distinctive (001) diffraction peak of the layered $PtSe_2$ (JCPDS PDF#: 01-088-2266) was observed, manifesting that $PtSe_2$ was grown along the *c*-direction without any other structures[36]. The detectable structural variations were rarely observed in either XRD or cross-sectional HRTEM, indicating that vdW layered structure still exists without significant deformation after the reaction (Supplementary Fig. 4a). Accordingly, EDS analysis exhibits that the ratio of Se to Pt is similar before and after the reaction with a change of less than 0.2 % (Supplementary Fig. 4b). As shown in Fig. 2e, two dominant phonon modes were detected by Raman spectroscopy: E_g (~179 cm^{-1}) and A_{1g} (~207 cm^{-1}) corresponding to the in-plane and out-of-plane vibration motions of top and bottom Se atoms inside a layer, respectively. Meanwhile, the intensity ratio between E_g and A_{1g} is around 4.1:1 (Fig. 2f, Supplementary Fig. 5). The peak positions and the intensity ratio of A_{1g}/E_g, similar to previous reports, indicating that vdW layer structure of $PtSe_2$ was horizontally established with high-quality[20,37,38]. Also, neither Raman spectroscopy nor the distribution map for the intensity ratio of A_{1g}/E_g reveals any meaningful variations.

Surface-exposed Pt and its role in CO oxidation

To identify the stability of atomically spread Pt species and their role in the CO oxidation reaction, we conducted an AP-XPS study in the synchrotron facility[39]. Considering the reaction conditions in Fig. 2, XPS was performed under four different environments: i) UHV at room temperature (RT), ii) near ambient pressure (NAP) at RT, iii) NAP at 200 °C, and iv) NAP at 250 °C. The NAP conditions were established with 0.3 mbar of CO and 0.7 mbar of O_2, following the pressure ratio of the reactions conducted in the UHV batch reactor.

Figure 3a displays the XPS core spectra of Pt 4*f* obtained under the four different environments. The photon energy is set to 760 eV. Considering the asymmetric degree and the instrumental signal

https://doi.org/10.1038/s41467-025-61320-0

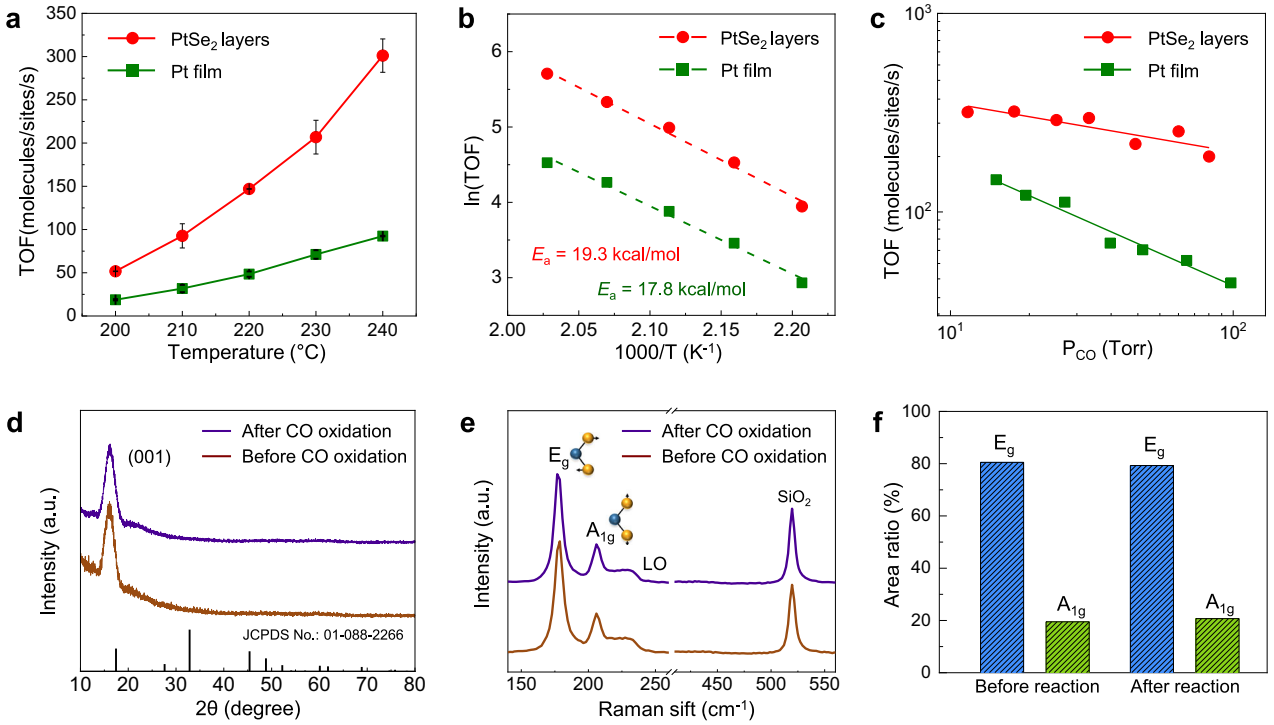

Fig. 2 | Catalytic performance and structural stability of $PtSe_2$ under CO oxidation. a TOF plots and **b** Arrhenius plots at elevated temperatures from 180 °C to 220 °C. Values (unit in kcal/mol) on the Arrhenius plot indicate the activation energy (E_a) of the CO oxidation reaction with each sample. Error bars represent standard deviations derived from the mean values of the 1st and 2nd experiments. **c** Kinetic study of the CO oxidation reaction as a function of the CO partial pressure with 100 Torr of O_2 at 210 °C. **d** XRD characterization of $PtSe_2$ before and after the CO oxidation reaction. **e** Raman profile and **f** area ratio of E_g (~179 cm^{-1}) and A_{1g} (~207 cm^{-1}) peaks before and after the CO oxidation reaction, calculated based on the Raman mapping data covering the 5 × 5 μm area represented in Supplementary Fig. 5.

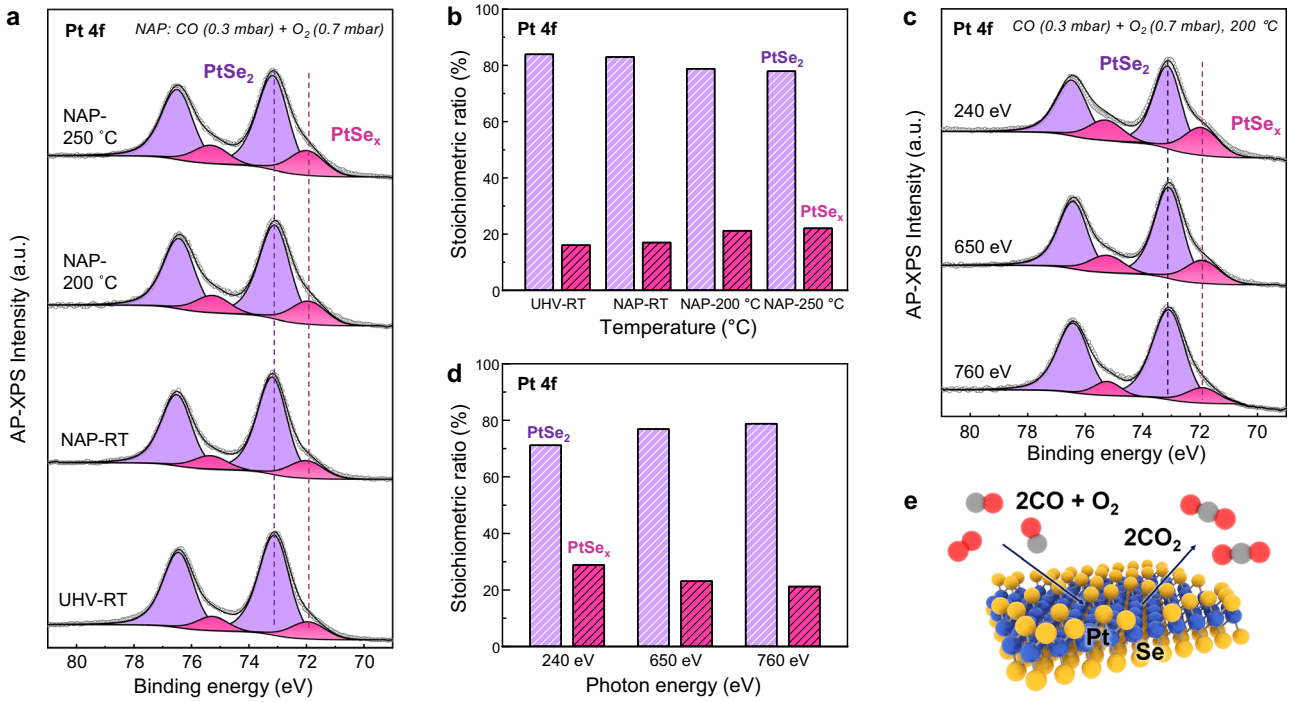

Fig. 3 | *Operando* characterizations of $PtSe_2$ via synchrotron radiation AP-XPS. a Pt 4*f* spectra under UHV-RT, NAP-RT, NAP-200 °C, NAP-250 °C using a photon energy of 760 eV. **b** The stoichiometric ratio of $PtSe_2$ and $PtSe_x$ spectrum under UHV-RT, NAP-RT, NAP-200 °C, NAP-250 °C using a photon energy of 760 eV. **c** Pt 4*f* spectra acquired using a photon energy of 240, 650, and 760 eV under NAP-200 °C. **d** The stoichiometric ratio of $PtSe_2$ and $PtSe_x$ spectrum in Pt 4*f* spectra acquired using a photon energy of 240, 650, and 760 eV under NAP-200 °C. **e** Reaction scheme of CO oxidation reaction on $PtSe_2$ layer.

https://doi.org/10.1038/s41467-025-61320-0

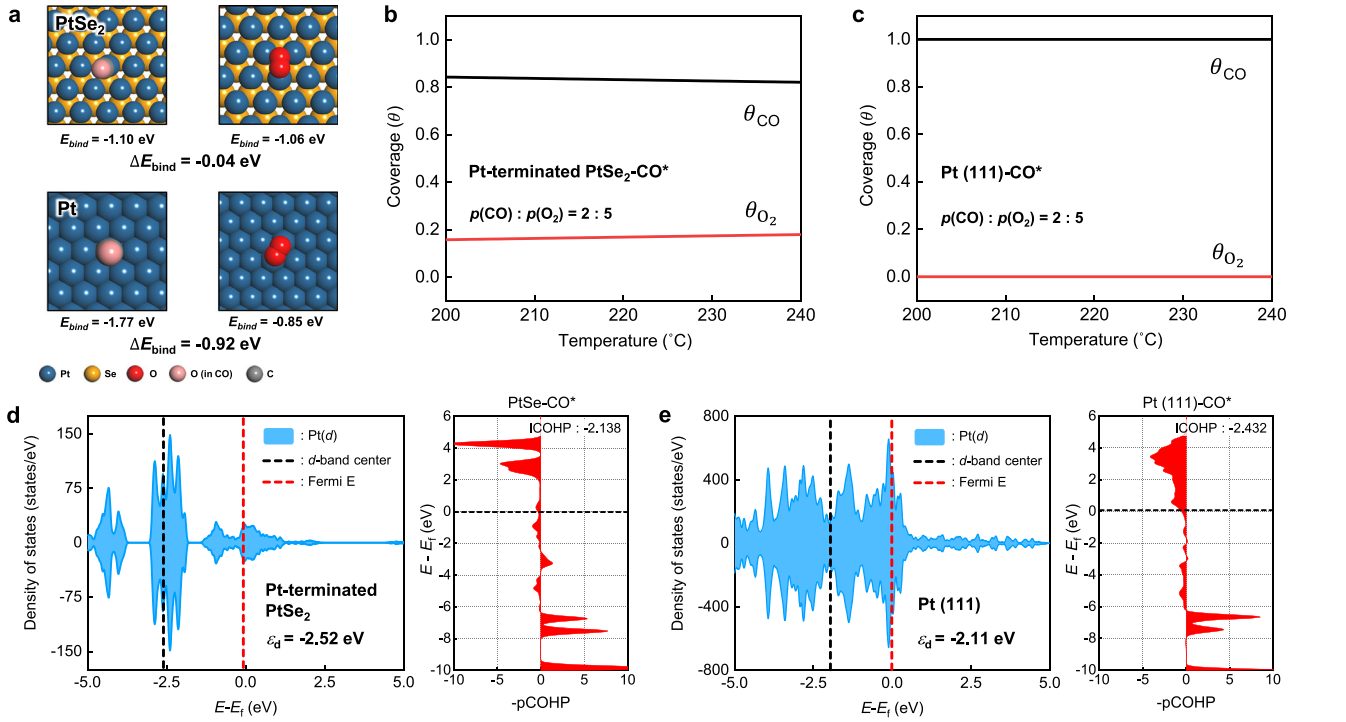

Fig. 4 | DFT calculations of CO and O_2 adsorption on Pt-terminated $PtSe_2$ and Pt(111). a The difference between CO and O_2 binding energy, ΔE_{bind}. Surface coverage diagrams of CO and O_2 on **b** Pt-terminated $PtSe_2$ and **c** Pt(111) under p(CO): $p(O_2)$ = 0.05: 0.013 (atm). Projected DOS (pDOS) diagrams and the location of ε_d, COHP, and integrated COHP (ICOHP) of **d** Pt-terminated $PtSe_2$ and **e** Pt(111), where E_f is the Fermi energy.

broadening error, the spectral envelope of Pt 4*f* can be attributed to the superposition of two different species, $PtSe_2$ and $PtSe_x$, where the spin-orbit splitting values and the weight ratio between spin-orbit peaks are set to 3.33 eV and 4:3, respectively. Li et al. investigated defects of $PtSe_2$ at the atomic scale and frequently found the presence of Se-vacancy on both the top and bottom Se sublayers in the $PtSe_2$ layer[22]. Since the formation energy of Se-vacancy is calculated to be between 1.55 and 1.85 eV within the Se chemical potential range of −0.35 to 0 eV, the authors addressed the frequent occurrence of Se-vacancy due to its low formation energy over a wide range of Se chemical potential. Therefore, in our XPS result, $PtSe_x$ $4f_{7/2}$ spectrum at 71.88 ± 0.03 eV is attributable to surface-exposed Pt species (i.e., Se-vacancy), while $PtSe_2$ $4f_{7/2}$ spectrum at 73.08 ± 0.03 eV corresponds to stoichiometric $PtSe_2$[40]. The spectral envelope of Se 3*d* spectra in Supplementary Fig. 6 can be similarly attributed to the superposition of $PtSe_2$ at 54.28 ± 0.04 eV and $PtSe_x$ at 54.71 ± 0.04 eV, with spin-orbit couple between $3d_{5/2}$ and $3d_{3/2}$. The spin-orbit splitting values and the weight ratio between spin-orbit peaks are set to 0.83 eV and 3:2, respectively. Detailed peak positions and area of Pt *4f* and Se *3d* spectra are organized in Supplementary Table 1.

The stoichiometric ratio of the $PtSe_x$ spectrum was 16.1 % at UHV-RT, 17.0% at NAP-RT, and gradually increased up to 22.1 % at NAP-250 °C (Fig. 3b). Se 3*d* spectra at the same environments also show a similar increasing trend. Several studies have reported that once mono Se-vacancy is sufficiently formed in $PtSe_2$, the migration of Se-vacancy and formation of multi vacancies can be preferably formed due to their high diffusivity[41–43]. Therefore, a slight increase of $PtSe_x$ spectrum during the reaction indicates that the adsorption of CO and O_2 on the surface-exposed Pt, along with the subsequent catalytic reactions, stabilizes the Pt and induces migration of Se-vacancy. In addition, structural analysis and stability tests on the catalytic ability confirm that Se-vacancy migration does not lead to any structural deformation or catalytic activity degradations (Fig. 2d–f, Supplementary Figs. 2 and 3).

Then, the thickness dependency of Se-vacancy was investigated by manipulating the penetration depth of the photon beam. After fixing the beam spot at a specific point, we sequentially acquired core spectra of $PtSe_2$ using three different photon energies ($h\nu$ = 240, 650, and 760 eV) under NAP-200 °C (Fig. 3c). The relative area intensity between the $PtSe_x$ and $PtSe_2$ spectra exhibits a clear increase with decreasing photon energy, varying from 21.2 % at 760 eV to 28.8 % at 240 eV (Fig. 3d). The distinct variation indicates that Pt species corresponding to $PtSe_x$ are predominantly present at the surface rather than in the sub-surface[44]. Specifically, by considering the electron attenuation length together with the variation in the area ratio between the $PtSe_x$ and $PtSe_2$ spectra, the Pt-to-Se ratio in the topmost layer was estimated to be 1:1.75 (± 0.05). Similar photon energy dependencies were observed for Pt 4*f* and Se 3*d* under all four different reaction conditions, corroborating that more Se-vacancy is mainly present at the surface (Supplementary Figs. 6 and 7). Therefore, it is inferred that a substantial fraction of Pt species is dispersed on the surface, serving as catalytically active sites (Fig. 3e).

Effect of Pt-Se charge transfer on the reaction mechanism

We performed DFT calculations to provide further insight into the improved activity of CO oxidation on $PtSe_2$, referring to the AP-XPS analysis. Such AP-XPS results indicate that the $PtSe_2$ layer has Se- and Pt-terminated adsorption sites. Therefore, we constructed two catalyst models: a Se-terminated $PtSe_2$ referring to the pristine $PtSe_2$ monolayer and a Pt-terminated $PtSe_2$ by exfoliating the topmost Se layer of the pristine $PtSe_2$ monolayer (Supplementary Fig. 8). The calculated binding energies (E_{bind}) of CO (−0.10 eV) and O_2 (−0.11 eV) on Se-terminated $PtSe_2$ indicate that Se sites cannot effectively bind the reactants (Supplementary Fig. 9). On the other hand, the E_{bind} of CO (−1.77 eV and −1.10 eV) and O_2 (−0.85 eV and −1.06 eV) on Pt(111) and Pt-terminated $PtSe_2$ indicate that Pt sites initiate CO oxidation (Fig. 4a). Since Se sites do not participate in CO oxidation, we used the Pt-

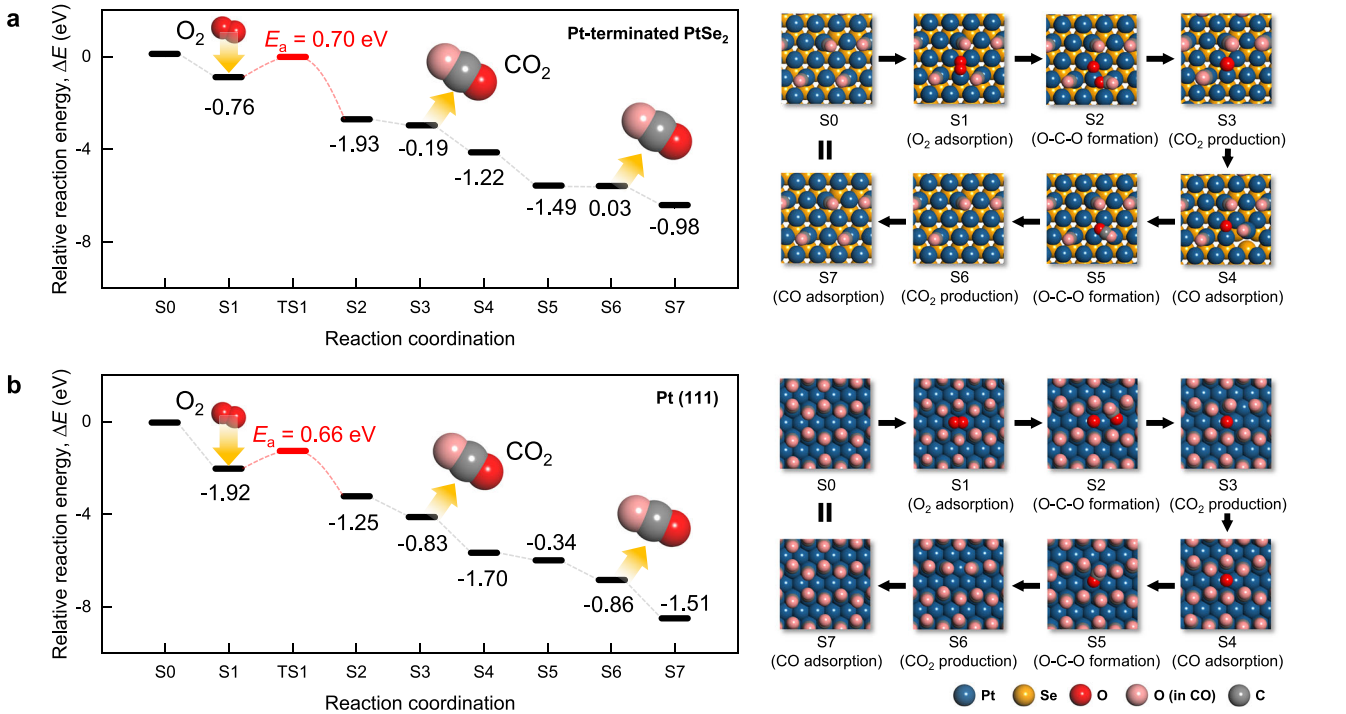

Fig. 5 | DFT-estimated CO oxidation pathway and energetics. a Pt-terminated $PtSe_2$ and **b** Pt(111). The numerical energy values below each state denote the relative reaction energy of the n^{th} step calculated by $\Delta E_n = E_n - E_{n-1}$.

terminated $PtSe_2$ model to study the catalytic activity of the Pt sites of $PtSe_2$.

Even a slight difference of around 0.1 eV between the E_{bind} of CO and O_2 may make a single adsorbate exclusively cover the catalyst surface[45]. In this manner, the large ΔE_{bind} ($\Delta E_{bind} = E_{bind}$ (CO) − E_{bind} (O_2)) of Pt(111) (−0.92 eV) makes the Pt(111) poisoned by CO (Fig. 4c). On the other hand, the marginal ΔE_{bind} of −0.04 eV calculated in Pt-terminated $PtSe_2$ indicates that competitive adsorption between CO and O_2 is available. The Langmuir adsorption isotherm in Fig. 4b shows that the O_2 coverage of the Pt-terminated $PtSe_2$ is about 20 % under the experimental CO oxidation condition. Our DFT calculation results suggest that the coverage issue accompanies the experimental findings in Fig. 2c, which elucidates the ability of $PtSe_2$ to exhibit high TOF and resistance to the CO poisoning effect due to the sufficient adsorption of oxygen.

It is well known that the transition metal surface with the higher ε_d generally more strongly binds an adsorbate, keeping the antibonding states empty[45]. The partial density of states (DOS) diagrams of Pt(111) and Pt-terminated $PtSe_2$ show that the ε_d decreases from −2.11 eV to −2.52 eV upon introducing Se, suggesting that the Pt-CO interaction in $PtSe_2$ is relatively weak (Fig. 4d, e). Besides, the crystal orbital Hamilton population (COHP) analysis results also present the relatively prominent antibonding states near the Fermi level of Pt-terminated $PtSe_2$, originating from downshifting of the $2\pi^*$ and $5\sigma^*$ orbitals of gas-phase CO upon adsorption (Supplementary Fig. 10). The increased integrated COHP value in Pt-terminated $PtSe_2$ (−2.183) compared with Pt(111) (−2.432) indicates that the antibonding becomes dominant. Our DFT calculation results concurrently suggest that the modulated electronic structure of $PtSe_2$ adjusts the adsorption trend of $PtSe_2$ to be beneficial for facile CO oxidation.

The DFT-calculated energetics of the overall CO oxidation reaction via the LH mechanism on Pt-terminated $PtSe_2$ and Pt(111) are presented in Fig. 5. The morphologies of the initial reaction stage, S0, are determined based on the equilibrium CO coverage (Supplementary Note 1). The morphologies on S1 to S3 show the formation of the O-C-O type intermediate by the interaction between CO and oxygen adsorbed on adjacent Pt sites, elucidating that densely distributed Pt sites on $PtSe_2$ enable CO oxidation through the LH mechanism. The reactions on Pt-terminated $PtSe_2$ and Pt(111) require 0.70 eV and 0.66 eV of activation energy barrier, respectively. These values reproduce the experimental apparent activation energy barriers presented in Fig. 2b. Subsequent CO_2 production from the O-C-O intermediate is exothermic in both cases ($\Delta E = -0.19$ eV in Pt-terminated $PtSe_2$ and −0.83 eV in Pt(111), respectively). After the first oxidation cycle, the residual oxygen atom readily oxidizes the second CO molecule[46,47].

Discussion

This study establishes atomically dispersed Pt on the surface of $PtSe_2$ as a high-performance heterogeneous catalyst for CO oxidation, providing the first experimental and theoretical evidence of its activity in gas-phase reactions. The $PtSe_2$ catalyst exhibited superior catalytic performance compared to a Pt film, which is attributed to the unique structural and electronic properties of the atomically dispersed Pt on $PtSe_2$.

Operando AP-XPS analysis identified surface-exposed Pt atoms of $PtSe_2$ and clarified their role as active sites. In addition, DFT calculations demonstrated that charge transfer within the Pt-Se bond modulates the *d*-band structure of Pt within $PtSe_2$, resulting in comparable binding energies of CO and O_2. Integrated analysis with CO partial pressure-dependent experiments confirmed the balanced adsorption behavior of CO and O_2 on $PtSe_2$. This behavior facilitates the adsorption of O_2 and leads to significantly higher oxygen coverage on $PtSe_2$ than on the Pt film, ultimately accelerating CO oxidation and enhancing catalytic performance. We also demonstrated that the dense distribution of Pt atoms on the $PtSe_2$ surface significantly contributes to the observed catalytic enhancement. Arrhenius analysis and DFT calculations revealed that high-density reaction sites promote the CO oxidation reaction via the LH mechanism.

Overall, these findings reveal that the outstanding catalytic performance of $PtSe_2$ stems from the synergistic interplay between electronic metal-chalcogen interactions and the high-density of atomically

dispersed Pt sites, which collectively facilitate efficient O_2 adsorption and promote favorable reaction pathways. Importantly, these characteristics are not exclusive to $PtSe_2$ and can be generalized to other TMDs with varied metal-chalcogen pairings. Furthermore, the ability to tune adsorbate binding energies suggests broader applicability of this approach to a range of gas-phase reactions beyond CO oxidation.

Methods

Fabrication of $PtSe_2$ multilayer and Pt film

$PtSe_2$ multilayer was synthesized using a horizontal quartz tube furnace (Lindberg/Blue M Mini-Mite) through CVD. The Pt seed with a thickness of 0.75 nm was deposited on SiO_2/Si wafers (~300 nm; SiO_2 thickness). The deposition was conducted using an e-beam evaporator (Thermionics VE-100) with a deposition rate of 0.05 Å/s. After deposition, Pt seed on SiO_2/Si substrate was placed in the central zone of the CVD furnace, while an alumina boat containing Se powder (99.99 %, Millipore Sigma) was positioned at the upstream side of the furnace at around 200 °C. For optimal growth conditions, the quartz tube was evacuated around 10 mTorr and purged with Ar gas to remove any residual molecules in it. After the evacuation, the furnace was heated to 400 °C for 50 minutes and then maintained for an additional 50 minutes. Throughout the growth process, the flow rate of Ar gas was maintained at around 200 standard cubic centimeters per minute at 100 mTorr[37].

Pt film with a thickness of 20 nm was deposited on the SiO_2/Si wafers (500 nm; SiO_2 thickness) using an e-beam evaporator (A-tech system). The deposition rate was 0.3 Å/s until the thickness reached 5 nm, then 0.7 Å/s until the thickness reached 20 nm, under 2.0 × 10^{-6} Torr. After deposition, Pt film was cooled down for 20 min under UHV conditions and for 1 hr under 760 Torr of N_2.

Catalytic performance measurements

Catalytic performance was measured in a batch reactor (1 L). The reactor was evacuated to UHV conditions (~10^{-8} Torr) using rotary and turbomolecular pumps. After that, CO, O_2, and He gases were sequentially injected into the reactor. To detect the reactants and products, a gas chromatograph (GC, Donam, DS 6200) equipped with a thermal conductivity detector was used. A stainless-steel molecular sieve 5 A (with a 0.5 nm nominal opening) was employed to separate the mixed gases. The mixed gases in the reactor were circulated through the reaction line at a rate of 2 L min^{-1} using a Metal Bellows recirculation pump (Senior Metal Bellows, MB-41) to synchronize the partial pressures within the reactor and GC. The reaction temperature was controlled using a ceramic boron nitride heater. A temperature controller provided feedback on the current applied to the heater, maintaining temperature fluctuations below 0.5 °C.

TOF (sec^{-1}) was calculated in terms of CO_2 produced per Pt active surface site per reaction time (sec), as shown in the following equation[26,48]:

$$Turnover\ frequency\ (TOF) = \frac{Turnover\ number(TON)}{Reaction\ time} = \frac{(CO\ conversion) \times \frac{P_{CO}V}{RT} \times N_A}{Pt\ active\ surface\ site \times Reaction\ time} \quad (1)$$

where P_{CO} is the partial pressure of CO (Torr), V is the volume of the batch chamber (L), R is the ideal gas constant (Torr·L/mol·K), T is the reaction temperature (K), and N_A is the Avogadro's number (mol^{-1}).

All the reaction data were obtained under low conversion conditions with a CO conversion rate below ~20%, assuming that the initial reaction rate was within a kinetically controllable regime. The number of active sites in the $PtSe_2$ was estimated based on the STEM images from the reference article[37].

Structural characterizations

XRD (RIGAKU, SmartLab) was performed to analyze the structural characteristics. Analysis was done on 2θ scan (grazing incidence of diffraction) mode with a scan speed of 5°/min and a step size of 0.01°. A structural image was obtained using TEM instrument (FEI, Titan cubed G2 60-300) capable of spherical aberration (Cs)-corrected HADDF-STEM and HRTEM imaging at 300 kV. The EDS mapping and count ratio between Pt and Se was analyzed using Super-X detector equipped on the same TEM instrument. A thin cross-section of $PtSe_2$ was prepared using a focused ion beam (FIB, Thermo Fisher Scientific, Helios G5 and FEI, Helios NanoLab 450 F1) with ~70 nm thickness for cross-sectional TEM analysis. Sample preparation with FIB was done after the carbon coating on the $PtSe_2$ and Pt film for protection. Raman spectroscopy (Horiba Jobin Yvon, ARAMIS) was performed to confirm the uniform growth and stability of $PtSe_2$. Phonon modes of samples were calibrated in reference to Si mode (~520 cm^{-1}).

Synchrotron-based analysis

Surface chemical states of $PtSe_2$ were analyzed via AP-XPS at the Pohang Accelerator laboratory (KBSI-PAL beamline, Pohang, South Korea)[39,49]. $PtSe_2$ was loaded under UHV (~10^{-12} bar) and then filled to near ambient pressure (10^{-3} bar). XPS data was calibrated with the C 1 s peak at 284.8 eV. Chemical bonding environment and oxidation state of $PtSe_2$ were analyzed via XAS Pt L3 edge spectra at the PAL 10 C beamline. $PtSe_2$ and Pt was loaded as film deposited on SiO_2/Si wafer, and PtO_2 was loaded as fine power (Platinum (IV) oxide, Sigma-Aldrich) using transparent tape (Scotch). XAS data was analyzed using Demeter software.

Computational details for density functional theory calculations

We constructed the three DFT models: Pt(111) 8×8×3, Se-terminated $PtSe_2$ 6×6×3, and Pt-terminated $PtSe_2$ 6×6×2 slabs. The Pt-terminated $PtSe_2$ model was constructed by exfoliating the topmost Se layer from the Se-terminated $PtSe_2$ 6×6×3 slab. This model was selected to emphasize the chemical factors that bring the experimentally observed catalytic functionality of $PtSe_2$. The Pt- and Se-terminated $PtSe_2$ models were designed to represent the surface morphology of the experimentally synthesized $PtSe_2$. All three models were used to study the CO oxidation activity comparatively. A 15 Å of vacuum space was added along the *z*-axis to avoid interference between the periodic supercells. All spin-polarized DFT calculations were conducted using the Vienna Ab-initio Simulation Package (VASP) code with the Perdew-Burke-Ernzerhof (PBE) exchange-correlation functional[50,51]. The interaction between the ionic core and valence electrons was described using the projector-augmented wave method[52]. Valance electron wave functions were expanded in a plane-wave basis set with an energy cutoff of 400 eV. The Brillouin zone was sampled at the Γ-point for all calculations. All electronic structure data was acquired using a 4×4×1 k-points sampling. Convergence criteria were set to 10^{-4} eV for the electronic structure and 0.05 eV/Å for the atomic geometry. A Gaussian smearing function with a finite temperature width of 0.05 eV was employed to enhance the convergence of states near the Fermi level. The location and energy of transition states were calculated using the climbing-image nudged-elastic-band (CI-NEB) method[53]. In addition, details about Langmuir adsorption models are described in Supplementary Note 2. Refer to Supplementary Note 3 for calculation quality test results.

Data availability

The data that support the finding of this study are available from the corresponding author upon reasonable request. Source data are provided with this paper.

References

1. Yang, X.-F. et al. Single-atom catalysts: a new frontier in heterogeneous catalysis. *Acc. Chem. Res.* **46**, 1740–1748 (2013).

2. Wang, A., Li, J. & Zhang, T. Heterogeneous single-atom catalysis. *Nat. Rev. Chem.* **2**, 65–81 (2018).
3. Zhu, Y. et al. Strain engineering of a defect-free, single-layer MoS_2 substrate for highly efficient single-atom catalysis of CO oxidation. *ACS Appl. Mater. Interfaces* **11**, 32887–32894 (2019).
4. Li, H. et al. Atomic structure and dynamics of single platinum atom interactions with monolayer MoS_2. *ACS Nano* **11**, 3392–3403 (2017).
5. Shi, Y. et al. Electronic metal-support interaction modulates single-atom platinum catalysis for hydrogen evolution reaction. *Nat. Commun.* **12**, 3021 (2021).
6. Lykhach, Y. et al. Counting electrons on supported nanoparticles. *Nat. Mater.* **15**, 284–288 (2016).
7. Liu, L. & Corma, A. Metal catalysts for heterogeneous catalysis: from single atoms to nanoclusters and nanoparticles. *Chem. Rev.* **118**, 4981–5079 (2018).
8. Lee, S. W. et al. Surface chemistry of hot electron and metal-oxide interfaces. *Surf. Sci. Rep.* **76**, 100532 (2021).
9. Liu, J. Catalysis by supported single metal atoms. *ACS Catal.* **7**, 34–59 (2017).
10. Yuan, W., Ma, Y., Wu, H. & Cheng, L. Single-atom catalysts for CO oxidation, CO_2 reduction, and O_2 electrochemistry. *J. Energy Chem.* **65**, 254–279 (2022).
11. Kumar, P. et al. High-density cobalt single-atom catalysts for enhanced oxygen evolution reaction. *J. Am. Chem. Soc.* **145**, 8052–8063 (2023).
12. Liu, X. et al. Superior catalytic performance of atomically dispersed palladium on graphene in CO oxidation. *ACS Catal.* **10**, 3084–3093 (2020).
13. Krishnan, R., Wu, S.-Y. & Chen, H.-T. Single Pt atom supported on penta-graphene as an efficient catalyst for CO oxidation. *Phys. Chem. Chem. Phys.* **21**, 12201–12208 (2019).
14. Li, Y., Zhou, Z., Yu, G., Chen, W. & Chen, Z. CO catalytic oxidation on iron-embedded graphene: computational quest for low-cost nanocatalysts. *J. Phys. Chem. C.* **114**, 6250–6254 (2010).
15. Luo, Y. et al. Unsaturated single atoms on monolayer transition metal dichalcogenides for ultrafast hydrogen evolution. *ACS Nano* **14**, 767–776 (2020).
16. Xuan, N. et al. Single-atom electroplating on two dimensional materials. *Chem. Mater.* **31**, 429–435 (2019).
17. Shi, Y. et al. Site-specific electrodeposition enables self-terminating growth of atomically dispersed metal catalysts. *Nat. Commun.* **11**, 4558 (2020).
18. Li, X., Rong, H., Zhang, J., Wang, D. & Li, Y. Modulating the local coordination environment of single-atom catalysts for enhanced catalytic performance. *Nano Res.* **13**, 1842–1855 (2020).
19. He, Y. et al. Amorphizing noble metal chalcogenide catalysts at the single-layer limit towards hydrogen production. *Nat. Catal.* **5**, 212–221 (2022).
20. Kim, J. H. et al. Revealing Pt-seed-induced structural effects to tribological/electrical/thermoelectric modulations in two-dimensional $PtSe_2$ using scanning probe microscopy. *Nano Energy* **91**, 106693 (2022).
21. Gong, Y. et al. Two-dimensional platinum diselenide: synthesis, emerging applications, and future challenges. *Nano Micro Lett.* **12**, 174 (2020).
22. Li, J. et al. Edge and point-defect induced electronic and magnetic properties in monolayer $PtSe_2$. *Adv. Funct. Mater.* **32**, 2110428 (2022).
23. Allian, A. D. et al. Chemisorption of CO and mechanism of CO oxidation on supported platinum nanoclusters. *J. Am. Chem. Soc.* **133**, 4498–4517 (2011).
24. Bunluesin, T., Cordatos, H. & Gorte, R. J. Study of CO oxidation kinetics on Rh/Ceria. *J. Catal.* **157**, 222–226 (1995).
25. Langmuir, I. The mechanism of the catalytic action of platinum in the reactions $2CO + O_2 = 2CO_2$ and $2H_2 + O_2 = 2H_2O$. *Trans. Faraday Soc.* **17**, 621–654 (1922).
26. Han, G., Song, H. C., Kim, S. H. & Park, J. Y. Role of the support oxidation state on the catalytic activity of two-dimensional Pt/TiO_x catalysts. *J. Phys. Chem. C.* **127**, 4096–4103 (2023).
27. Nørskov, J. K., Abild-Pedersen, F., Studt, F. & Bligaard, T. Density functional theory in surface chemistry and catalysis. *PNAS* **108**, 937–943 (2011).
28. Yu, X. et al. Atomically thin noble metal dichalcogenide: a broad-band mid-infrared semiconductor. *Nat. Commun.* **9**, 1545 (2018).
29. Ma, H. et al. Controlled synthesis of ultrathin $PtSe_2$ nanosheets with thickness-tunable electrical and magnetoelectrical properties. *Adv. Sci.* **9**, 2103507 (2022).
30. Zhang, L. et al. Precise layer-dependent electronic structure of MBE-grown $PtSe_2$. *Adv. Electron. Mater.* **7**, 2100559 (2021).
31. Dai, J. et al. Hydrogen spillover in complex oxide multifunctional sites improves acidic hydrogen evolution electrocatalysis. *Nat. Commun.* **13**, 1189 (2022).
32. Fang, S. et al. Uncovering near-free platinum single-atom dynamics during electrochemical hydrogen evolution reaction. *Nat. Commun.* **11**, 1029 (2020).
33. Shimizu, K. -i et al. Quantitative determination of average rhodium oxidation state by a simple XANES analysis. *Appl. Catal. B: Environ.* **111-112**, 509–514 (2012).
34. Zhu, Y. et al. Facilitating alkaline hydrogen evolution reaction on the hetero-interfaced Ru/RuO_2 through Pt single atoms doping. *Nat. Commun.* **15**, 1447 (2024).
35. Song, H. C. et al. Engineering nanoscale interfaces of metal/oxide nanowires to control catalytic activity. *ACS Nano* **14**, 8335–8342 (2020).
36. Zeng, L. et al. Ultrafast and sensitive photodetector based on a $PtSe_2$/silicon nanowire array heterojunction with a multiband spectral response from 200 to 1550 nm. *NPG Asia Mater.* **10**, 352–362 (2018).
37. Han, S. S. et al. Horizontal-to-vertical transition of 2d layer orientation in low-temperature chemical vapor deposition-grown $PtSe_2$ and its influences on electrical properties and device applications. *ACS Appl. Mater. Interfaces* **11**, 13598–13607 (2019).
38. Gulo, D. P., Yeh, H., Chang, W.-H. & Liu, H.-L. Temperature-dependent optical and vibrational properties of $PtSe_2$ thin films. *Sci. Rep.* **10**, 19003 (2020).
39. Kim, G. et al. AP-XPS beamline, a platform for *operando* science at Pohang accelerator laboratory. *J. Synchrotron Radiat.* **27**, 507–514 (2020).
40. Sojková, M. et al. High carrier mobility epitaxially aligned $PtSe_2$ films grown by one-zone selenization. *Appl. Surf. Sci.* **538**, 147936 (2021).
41. Gao, J. et al. Structure, stability, and kinetics of vacancy defects in monolayer $PtSe_2$: a first-principles study. *ACS Omega* **2**, 8640–8648 (2017).
42. Kumar, P., Meng, A. C., Jo, K., Stach, E. A. & Jariwala, D. Interfacial reaction and diffusion at the one-dimensional interface of two-dimensional $PtSe_2$. *Nano Lett.* **22**, 4733–4740 (2022).
43. Chen, J. et al. Atomic-level dynamics of point vacancies and the induced stretched defects in 2D monolayer $PtSe_2$. *Nano Lett.* **22**, 3289–3297 (2022).
44. Powell, C. J. Practical guide for inelastic mean free paths, effective attenuation lengths, mean escape depths, and information depths in X-ray photoelectron spectroscopy. *J. Vac. Sci. Tech.* **38**, 023209 (2020).
45. Hoffmann, R. *Solids and Surfaces: a Chemist's View of Bonding in Extended Structures*. (VCH Publishers, 1988).
46. Kim, H. Y., Lee, H. M. & Henkelman, G. CO oxidation mechanism on CeO_2-supported Au nanoparticles. *J. Am. Chem. Soc.* **134**, 1560–1570 (2012).
47. Kim, H. Y. & Liu, P. Complex catalytic behaviors of $CuTiO_x$ mixed-oxide during CO oxidation. *J. Phys. Chem. C.* **119**, 22985–22991 (2015).

48. Song, H. C. et al. Synergistic interactions between water and the metal/oxide interface in CO oxidation on Pt/CeO_2 model catalysts. *Catal. Today* **411-412**, 113825 (2023).
49. Kim, T.-S. et al. Catalytic boosting on AuCu bimetallic nanoparticles by oxygen-induced atomic restructuring. *Appl. Catal. B: Environ.* **331**, 122704 (2023).
50. Kresse, G. & Furthmüller, J. Efficiency of ab-initio total energy calculations for metals and semiconductors using a plane-wave basis set. *Comput. Mater. Sci.* **6**, 15–50 (1996).
51. Perdew, J. P., Burke, K. & Ernzerhof, M. Generalized gradient approximation made simple. *Phys. Rev. Lett.* **77**, 3865–3868 (1996).
52. Blöchl, P. E. Projector augmented-wave method. *Phys. Rev. B* **50**, 17953–17979 (1994).
53. Henkelman, G., Uberuaga, B. P. & Jónsson, H. A climbing image nudged elastic band method for finding saddle points and minimum energy paths. *J. Chem. Phys.* **113**, 9901–9904 (2000).

Acknowledgements

J.Y.P. and H.Y.K. acknowledge support from the National Research Foundation of Korea (NRF) grant funded by the Korean government (MSIT) (2022R1A2C3004242), (RS-2023-NR077216), (RS-2021-NR060128). Y. Jung acknowledges financial support from the US National Science Foundation (CAREER: 2142310). J.H.K. acknowledges the support from Inha University. S. S. Han acknowledges financial support from the Preeminent Postdoctoral Program (P3) at UCF. S.W.L. acknowledges the support from the Inha University Research Grant. Synchrotron-based AP-XPS research at the KBSI-PAL 8A2 AP-XPS beamline and XAS research at the 10C beamline were supported in part by Pohang Accelerator Laboratory/POSTECH and Korea Basic Science Institute under the R&D program (Project No. A426220) supervised by the Ministry of Science and ICT.

Author contributions

G.H., H.C., and J.H.K. contributed equally. G.H., J.H.K., and J.Y.P. conceptualized the research. S.S.H. performed the synthesis under the guidance of Y.J. G.H., D.K., H.P., K.K., J.K., and M.G.K. performed the characterizations and experimental analysis. G.H. performed the catalytic performance measurements. H.C. and H.Y.K. performed the theoretical analysis. G.H. and H.C. wrote the manuscript with feedback from all authors. J.H.K., S.W.L., and J.Y.P. provided major supervision.

Competing interests

The authors declare no competing interests.

Additional information

Supplementary information The online version contains supplementary material available at https://doi.org/10.1038/s41467-025-61320-0.

Correspondence and requests for materials should be addressed to Yeonwoong Jung, Hyun You Kim or Jeong Young Park.

Peer review information *Nature Communications* thanks Yu Jing and the other, anonymous, reviewers for their contribution to the peer review of this work. A peer review file is available.